Nano Research

Open Access

Research Article

Enhanced Li^+ transport across the organic–inorganic interface in composite solid electrolytes via a confined solvation strategy

Kai Chen[1], Mingjia Lu[1], Xiaoxiao Li[1], Feili Lai[4], Chao Zhang[1], Hiang Kwee Lee[3], Yue-E Miao[1] ✉, and Tianxi Liu[1,2] ✉

[1] *State Key Laboratory of Advanced Fiber Materials, College of Materials Science and Engineering, Donghua University, Shanghai 201620, China*
[2] *Key Laboratory of Synthetic and Biological Colloids, Ministry of Education, School of Chemical and Material Engineering, Jiangnan University, Wuxi 214122, China*
[3] *Division of Chemistry and Biological Chemistry, School of Chemistry, Chemical Engineering and Biotechnology, Nanyang Technological University, Singapore 637371, Singapore*
[4] *State Key Laboratory of Metal Matrix Composites, School of Materials Science and Engineering, Shanghai Jiao Tong University, Shanghai 200240, China*

Cite this article: *Nano Research*, **2025**, *18*, 94907388. https://doi.org/10.26599/NR.2025.94907388

ABSTRACT: Polymer-based composite solid electrolytes (CSEs), incorporating fast Li^+-conducting ceramic phases, leverage the advantages of both components to become one of the most promising next-generation solid electrolyte configurations. However, the interfacial incompatibility between the organic and inorganic components inevitably creates significant barriers to the interfacial Li^+ transport, representing a key challenge in further enhancing the ionic conductivity of CSEs. Herein, we pioneered a confined solvation strategy by growing a metal-organic framework (MOF) layer impregnated with ionic liquid (IL) on the surface of $Li_{0.33}La_{0.557}TiO_3$ (LLTO) fibers, and subsequently incorporating the composite fibers into a polyethylene oxide (PEO) matrix to fabricate a novel CSE (signed as LLTO/ZIF-8@IL/PEO). Benefiting from the unique porous structure and attraction of the metal centers toward anions of MOF, IL is tightly confined within the MOF framework, while retaining its liquid-like high ionic conductivity and interfacial wetting ability at the nano scale. As a result, the Li^+ transport efficiency is substantially improved across the PEO-LLTO fiber interface to enable a high ionic conductivity of 1.07×10^{-3} $S \cdot cm^{-1}$ at 60 °C for LLTO/ZIF-8@IL/PEO. The corresponding pouch cell with a $LiFePO_4$ (LFP) cathode (22 mg loading) and a lithium metal anode can successfully charge a mobile phone and deliver a stable capacity of 135.02 $mAh \cdot g^{-1}$ at 0.2 C over 100 cycles. This confined solvation strategy offers a universal and efficient approach for improving the Li^+ transport across the polymer-ceramic interface in CSEs.

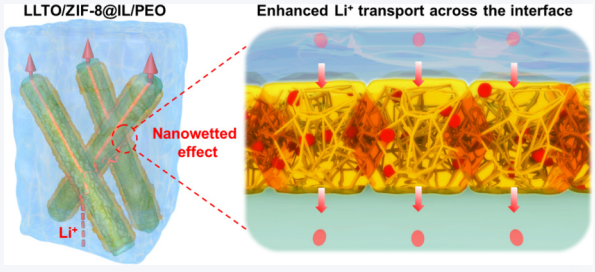

KEYWORDS: composite solid electrolytes, interfacial lithium-ion transport, organic–inorganic interface, metal-organic framework, ionic liquid

1 Introduction

The composite solid electrolytes (CSEs), prepared by incorporating ceramic fillers with fast Li^+-conducting ability into polymer electrolytes, can theoretically resolve the issue of low ionic conductivity in polymer electrolytes while retaining the advantages of easy processing and good electrode contact, serves as a potential breakthrough for achieving performance leaps in next-generation solid-state lithium batteries [1–9]. However, compared to the CSEs blended with non-conductive fillers, numerous studies have shown that CSEs incorporating fast Li^+-conducting fillers fail to achieve the anticipated significant improvement in ionic conductivity [10, 11]. In other words, the potential of these fast Li^+-conducting ceramics has not been fully exploited [12, 13]. Instead, they primarily perform functions similar to those of non-conductive fillers, such as reducing the crystallinity of the polymer matrix [14] and promoting the dissociation of local lithium salts through Lewis acid-base interactions at the organic–inorganic interfaces [15].

Many researchers have identified that a key factor contributing to the unsatisfactory performance of CSEs is the considerable barrier of Li^+ transport across the organic–inorganic interface [16–19]. Typically, during the preparation of CSEs, some fast Li^+-

Received: March 3, 2025; **Revised:** March 17, 2025
Accepted: March 18, 2025

✉Address correspondence to Yue-E Miao, yuee_miao@dhu.edu.cn; Tianxi Liu, txliu@jiangnan.edu.cn

conducting inorganic fillers are exposed to air, forming an inert oxide layer [20]. Moreover, when the inorganic fillers contact with the polymer electrolytes, lithium salts, and solvents, they tend to undergo a series of complex side reactions, resulting in the formation of an inert layer composed of inorganic decomposition products [21]. These inert layers fail to efficiently transport Li^+ between the two phases, consequently reducing the overall ionic conductivity of CSEs. In addition, these side reactions often involve structural changes in the polymer phase, which also weaken the Li^+ transport capability across the interface. For example, in the polyethylene oxide (PEO) electrolyte matrix, an oxygen-depleted layer formed near the interface of the fast Li^+-conducting fillers due to the excessive consumption of oxygen atoms, could further hinder the Li^+ exchange between the organic and inorganic phases [22].

To overcome the Li^+ transport obstacle at the organic–inorganic interphase in CSEs, the most direct approach is to try to eliminate the inert inorganic layer. Methods such as high-temperature treatment and chemical etching have been reported to effectively remove the inert layer [18, 20]. To prevent the reformation of the layer, surface modifiers like polydopamine were also employed to inhibit the occurrence of undesirable reactions [23]. Furthermore, other surface modifiers like succinic anhydride have been developed that could not only prevent the formation of inorganic layers but also enhance the Li^+ transport at the interface [24]. Although these strategies have improved the Li^+ transport efficiency across the different interface to a large extent, the underlying mechanism of the ion transfer process still remains being across a solid–solid interface, which presents inherent disadvantages when compared to the ion transport across a solid–liquid interface. Ionic liquids (ILs), characterized by high ionic conductivity, wide electrochemical window, and excellent safety of non-flammability and non-volatility, have been extensively utilized in battery research and regarded as ideal liquids to wet the organic–inorganic interfaces in CSEs [25–31]. However, a lot of studies merely involve the simple addition of ILs into CSEs during the fabrication process, leading to a widespread distribution of ILs throughout the polymer matrix, which severely reduced their effectiveness as interfacial modifiers [17, 32]. Although some researchers have successfully utilized the incompatibility between specific ILs and polymers to achieve the distribution of ILs on the surface of the ceramic phase in CSEs [22], the conditions for achieving this selective distribution of ILs are too strict and could hardly be applicable to all types of ILs and polymers.

Herein, we developed a universal confined solvation strategy for CSEs that transforms the challenging ion transport across the solid–solid interfaces into stable and efficient ion transport across the solid–liquid interfaces. Through growing a uniform layer of ZIF-8 particles on the surface of $Li_{0.33}La_{0.557}TiO_3$ (LLTO) fibers and impregnating ZIF-8 particles with an IL containing lithium salt (IL-Li), followed by infusion of a PEO electrolyte, a novel CSE, denoted as LLTO/ZIF-8@IL/PEO, can be obtained in this work. Owing to the high specific surface area endowed by the three-dimensional porous structure and the abundant metal centers of ZIF-8 particles exhibiting Lewis acid characteristics, LLTO/ZIF-8@IL/PEO can effectively serve as a reservoir to tightly absorb IL-Li at the ZIF-8 decorated PEO-LLTO interface and prevent it from diffusing into the PEO matrix. The confined solvation layer of ZIF-8@IL exerts a nanoscale interfacial wetting effect on both the PEO and LLTO fibers, acting as a bridge to facilitate the efficient ion exchange between the two phases as confirmed by ^7Li-^7Li two-dimensional exchange spectroscopy (2D-EXSY) nuclear magnetic resonance (NMR). As a result, LLTO/ZIF-8@IL/PEO exhibits a high ion conductivity of 1.07×10^{-3} S·cm^{-1} at 60 °C. Both the Li||Li symmetric cell and $LiFePO_4$ (LFP)||Li full cell assembled with LLTO/ZIF-8@IL/PEO exhibit excellent cycling stability, further demonstrating the effectiveness of the confined solvation strategy in enhancing Li^+ transport across the polymer-ceramic interface for improved performance of the CSEs.

2 Experimental

2.1 Materials and chemicals

All battery-related materials, including carbon-coated aluminum foil, Super P LI carbon black, CR2025 coin cell cases, aluminum-plastic film and current collector for pouch cells, $LiFePO_4$ (LFP) cathode material, $LiCoO_2$ (LCO) cathode material, lithium disks for coin cells (diameter: 14 mm, thickness: 300 μm), and lithium foils for pouch cells (58 mm × 45 mm, thickness: 100 μm), were purchased from Shenzhen Kejingstar (MTI) Technology Co., Ltd. The commercial liquid electrolyte (LE) was 1 mol·L^{-1} lithium bistrifluoromethane sulfonamide (LiTFSI) salt in 1,3-dioxolane/1,2-dimethoxyethane (1:1, v/v) with 2 wt.% $LiNO_3$, which was purchased from Duoduo chemical company in Suzhou. The polyester non-woven fabric FPC3018 for batteries was supplied by Mitsubishi Paper Mills Ltd. All other reagents used in this work were purchased from Aladdin Biochemical Technology Co., Ltd. (Shanghai, China) and employed as received, without any additional purification.

2.2 Preparation of LLTO fibers

Briefly, $Ti(OC_4H_9)_4$, $La(NO_3)_3{\cdot}6H_2O$, and $LiNO_3$ (15 wt.% excess) of various corresponding molar mass were successively dissolved in a transparent solution by mechanical stirring in a 60 °C oil bath using *N*,*N*-dimethylformamide (DMF) as solvent which consisted of 10 wt.% acetic acid and 14 wt.% polyvinyl pyrrolidone (PVP, M_W = 1,300,000). Then, the above spinning solution was transferred into two 10 mL syringes and electrospun for 10 h to obtain the LLTO precursor fibers. The detailed parameters were set as follows: The distance between two needle tips and the collector was fixed at 15 cm, the injection speed was 0.01 mL·min^{-1} for both syringes combined with a voltage of 15 kV, and the speed of the collecting roller was set to 80 rpm. Then, the LLTO precursor fibers were transferred to a tube furnace exposed to air for sintering to produce the LLTO fibers. The sintering process was as follows: The sample was heated from 30 to 100 °C after 40 min, and then to 600 °C after 370 min, followed by an increase to 800 °C after 70 min. It was further held at 800 °C for 10 h, and finally allowed to cool naturally.

2.3 Preparation of LLTO/ZIF-8@IL/PEO

The obtained LLTO fibers were immersed in a 50 mL methanol solution containing 1.5 g of $Zn(NO_3)_2{\cdot}6H_2O$ (signed as solution A). Meanwhile, a 50 mL methanol solution containing 4 g of 2-methylimidazole was prepared and signed as solution B. The solution of A and B was heated at 55 °C for 1 h, respectively. Afterward, the solution B was added into the solution A and mixed thoroughly, and the reaction was allowed to proceed overnight at 55 °C to obtain the LLTO fibers with ZIF-8 particles grown on their surface (denoted as LLTO/ZIF-8). Then, the LLTO/ZIF-8 fibers

were washed three times with methanol, and transferred to a vacuum oven at 120 °C overnight to remove excess solvent. During this process, the white precipitate of ZIF-8 particles was also collected during the washes for subsequent characterization. Subsequently, the LLTO/ZIF-8 was transferred to a hot plate set at 140 °C and sprayed with an equal mass of a solution, denoted as IL-Li, containing 20 wt.% LiTFSI in 1-ethyl-3-methylimidazolium bis(trifluoromethylsulfonyl)imide (EMIM-TFSI) using a spray device. The mixture was then left to stand overnight to ensure full absorption, yielding LLTO/ZIF-8@IL. This approach above for uniformly loading the IL-Li is referred to as the hot-spray method. The obtained LLTO/ZIF-8@IL was then incorporated with PEO (M_W = 600,000) through infusing an acetonitrile solution containing PEO and LiTFSI at a mass ratio of 9:1. After the acetonitrile completely evaporated, the membrane was finally cut into disks with a diameter of 16 mm to obtain the LLTO/ZIF-8@IL/PEO electrolyte. For comparison, we also prepared several CSEs of LLTO/PEO, LLTO/ZIF-8/PEO, and LLTO/PEO-IL, formed by incorporating LLTO fibers with PEO, LLTO/ZIF-8 with PEO, and LLTO with PEO and IL-Li, respectively. The contents of LLTO, ZIF-8, and IL-Li in these samples were controlled to match those in LLTO/ZIF-8@IL/PEO. Notably, during the preparation of the LLTO/PEO-IL sample, the hot-spray method was also employed to achieve the uniform deposition of IL-Li onto the LLTO structure prior to its integration with PEO.

2.4 Materials characterizations

Scanning electron microscope (SEM) images of all samples were captured by JEOL JSM 7500F. The X-ray diffraction (XRD) patterns were characterized by Bruke D8 Advance using a Cu-Kα source (λ = 1.54 Å). Thermogravimetric analyses (TGA) curves were measured through NETZSCH TG209F1 Libra at a heating rate of 10 °C·min^{-1} in an air atmosphere. Differential scanning calorimetry (DSC) curves were investigated via PerkinElmer DSC 4000 at a fixed heating or cooling rate of 2 °C·min^{-1}. The stress–strain tests were conducted on an electromechanical test system (SANS UTM2102) at a stretching speed of 10 mm·min^{-1}. N_2 sorption isotherms at 77 K for all samples were analyzed through a Quantachrome Autosorb-iQ-AG porosimeter. The contact angles of different samples with IL-Li were measured by a contact angle meter (DatePhysics OCA40). Fourier transform infrared (FTIR) spectra were characterized through Perkin Elmer Spectrum BX Ⅱ (equipped with ATR accessory).

2.5 Electrochemical characterizations

All the cells were assembled in a glovebox filled with Ar (H_2O < 0.1 ppm, O_2 < 0.1 ppm) and sealed in CR2025 coin cell cases or aluminum-plastic films. Electrochemical impedance spectroscopy (EIS), chronoamperometry (CA), and linear sweep voltammetry (LSV) tests were carried out using a DH7000 electrochemical workstation (Jiangsu Donghua Analytical Instrument Co., Ltd.). For all EIS measurements, the frequency range was set from 1 Hz to 1 MHz, with an applied amplitude of 10 mV. The ionic conductivities (σ) of different electrolytes were characterized through EIS measurements on a cell configuration of stainless steel (SS)||electrolyte||SS and calculated by the following equation

$$\sigma = \frac{L}{S \times R} \quad (1)$$

where L (cm) represents the thickness of the electrolyte (~ 200 μm), R (Ω) is the bulk resistance, and S (cm^2) denotes the contact area between the SS and the electrolyte. The temperature-dependent ionic conductivity was fitted with the Arrhenius equation to calculate the activation energy (E_a) of the electrolyte

$$\sigma = A \times \exp\left(\frac{E_a}{k_b \times T}\right) \quad (2)$$

where A stands for the pre-exponential factor, k_b stands for the Boltzmann constant, and T stands for the absolute temperature. CA tests were conducted by applying a constant voltage of 10 mV to the cell and recording the corresponding current as it gradually stabilized. The Li^+ transference number (t_{Li^+}) was calculated using the following equation

$$t_{Li^+} = \frac{I_s \times R_{b0} \times (\Delta V - I_0 \times R_{i0})}{I_0 \times R_{bs} \times (\Delta V - I_s \times R_{is})} \quad (3)$$

where I_0 and I_s represent the initial and steady currents during polarization, R_{b0} and R_{i0} are the initial bulk resistance and interfacial resistance, and R_{bs} and R_{is} are the steady bulk resistance and interfacial resistance. LSV curves of different electrolytes were recorded using a cell configuration of Li||electrolyte||SS over a voltage range of 2.5 to 6 V with a scan rate of 0.5 mV·s^{-1}. Galvanostatic charge/discharge tests for all Li||electrolyte||Li symmetric coin cells, Li||electrolyte||LFP coin cells and pouch cells, and Li||electrolyte||LCO full cells were tested at 60 °C based on a NEWARE battery testing system (MIHW-200-160CH-B, Shenzhen Neware Electronics Co., Ltd.). To prevent side reactions between lithium metal and LLTO, a barrier composed of a non-woven fabric FPC3018 membrane and PEO was placed between all LLTO-containing electrolytes and lithium metal in these batteries. In addition, during the assembly of Li||electrolyte||LFP or LCO coin cells and Li||electrolyte||LFP pouch cells, 5 and 100 μL of LE were injected at the interface between the electrolyte and the cathode, respectively, to enhance the electrochemical performance. For the cathode preparation, LFP or LCO powder, super P LI carbon black, and PEO were mixed in a weight ratio of 7:2:1 in 1-methyl-2-pyrrolidone. The resulting slurry was coated onto a carbon-coated aluminum foil, followed by drying at 80 °C in a vacuum oven overnight. The coated foil was then punched into 12 mm disks with a mass loading of 0.5–1.0 mg·cm^{-2} for coin cells and 57 mm × 44 mm rectangular sheets with a mass loading of 22 mg for pouch cells.

3 Results and discussion

As depicted in Fig. 1, in the traditional CSEs without any optimizations, the formation of inorganic decomposition products easily leads to a poor organic–inorganic interface, which largely hinders the Li^+ transfer from the PEO matrix into the LLTO fibers and leads to the slow ion transport. On the contrary, in LLTO/ZIF-8@IL/PEO, the interface between LLTO and PEO is nanowetted by the confined solvation layer of ZIF-8@IL, which can significantly enhance the Li^+ transport across the organic–inorganic interface. Therefore, Li^+ can efficiently migrate from the PEO into the LLTO fiber network, taking advantage of the inherent high ionic conductivity of LLTO to boost the overall ionic conductivity of CSEs.

Figure 2(a) illustrates the detailed fabrication process of LLTO/ZIF-8@IL/PEO and the corresponding SEM images can be seen in Figs. 2(b)–2(g). Compared to the LLTO fibers (Fig. 2(b)),

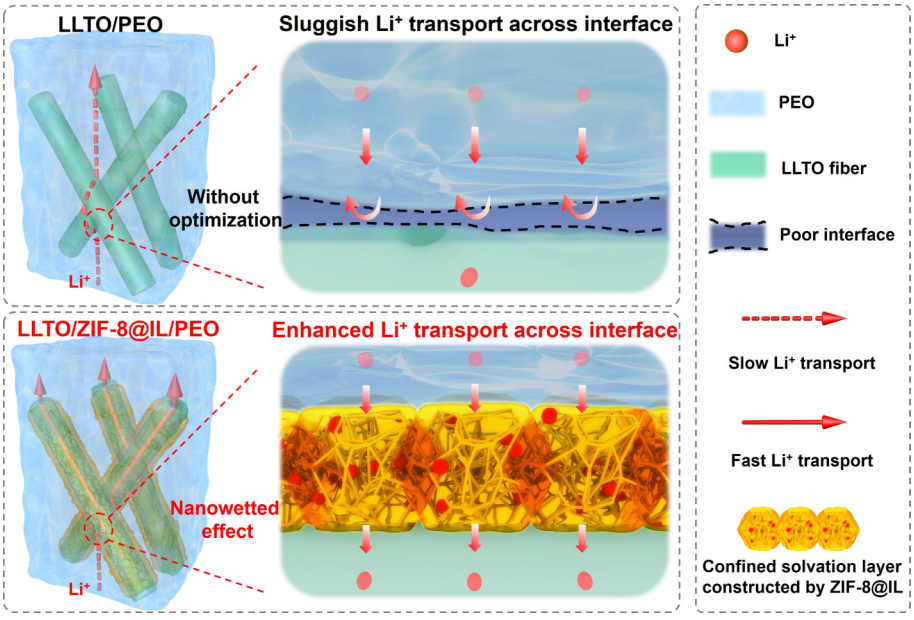

Figure 1 Schematic illustration of the nanowetted effect of the confined solvation strategy.

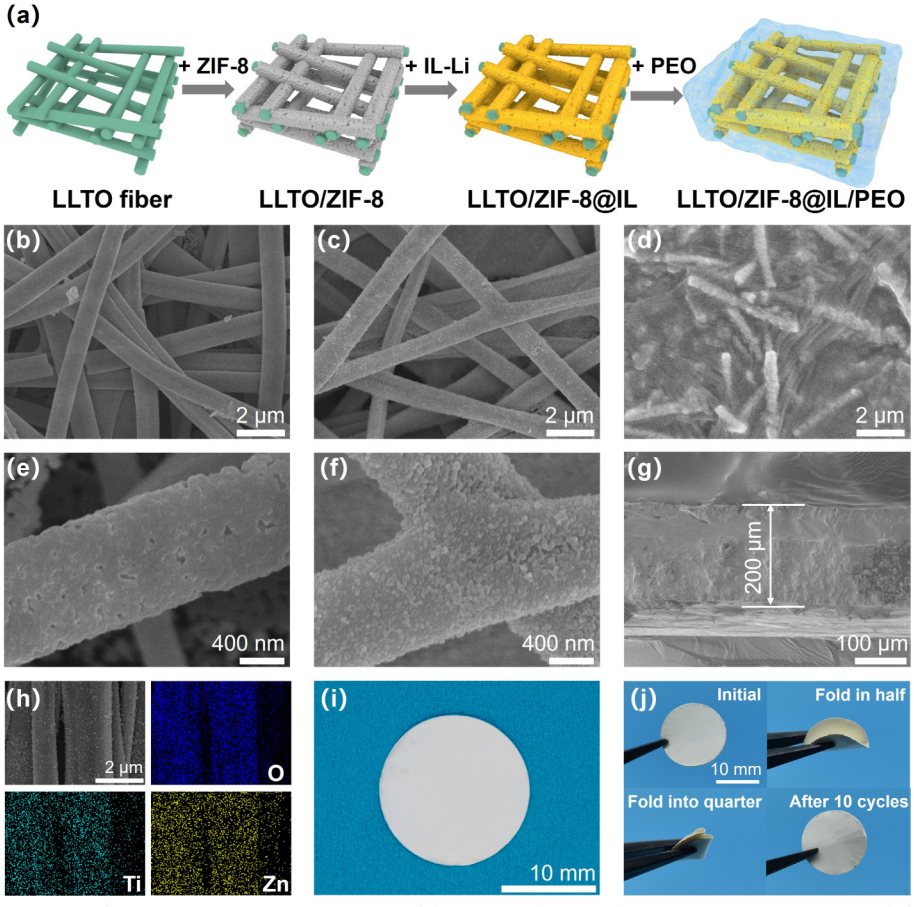

Figure 2 (a) The fabrication process of LLTO/ZIF-8@IL/PEO. SEM images of (b) LLTO and (e) an enlarged view, (c) LLTO@ZIF-8 and (f) an enlarged view, and (d) LLTO/ZIF-8@IL/PEO and (g) a cross-sectional view. (h) EDS elemental mapping images of LLTO/ZIF-8. Digital photographs showing the (i) appearance and (j) flexibility and mechanical stability of LLTO/ZIF-8@IL/PEO.

the LLTO/ZIF-8 exhibits a rougher morphology after the growth of ZIF-8 particles on the fiber surface (Fig. 2(c)). At higher magnification, it is observed that LLTO fibers are primarily composed of tightly stacked LLTO crystals (Fig. 2(e)). In contrast, a layer of densely packed small particles is clearly visible on the surface of LLTO fibers in the enlarged SEM image of LLTO/ZIF-8 (Fig. 2(f)). Further analysis using energy dispersive X-ray spectroscopy (EDS) reveals that the distribution of Zn element in

LLTO/ZIF-8 closely overlaps with the representative elements of Ti and O elements in LLTO (Fig. 2(h) and Fig. S1 in the Electronic Supplementary Material (ESM)), confirming the successful fabrication of LLTO/ZIF-8. Figure 2(d) shows the surface morphology of LLTO/ZIF-8@IL/PEO, where IL-Li-absorbed LLTO/ZIF-8 is firmly embedded within the PEO matrix. The compact structure of LLTO/ZIF-8@IL/PEO is further confirmed by the cross-sectional SEM image in Fig. 2(g), which reveals a thickness of approximately 200 μm being in good agreement with the measurement obtained using a thickness gauge (Fig. S2 in the ESM). Finally, the digital photograph taken from the top view (Fig. 2(i)) shows that LLTO/ZIF-8@IL/PEO has a white appearance. Moreover, as illustrated in Fig. 2(j), LLTO/ZIF-8@IL/PEO demonstrates excellent flexibility and mechanical stability, retaining its structural integrity even after 10 repeated folding cycles.

The XRD patterns are acquired in Fig. 3(a). The diffraction peaks of ZIF-8 align perfectly with the simulated results, while the diffraction peaks of LLTO at 2θ = 32.6°, 40.3°, 46.9°, 58.3°, and 68.5° also match well with those in the JCPDS card. Besides, the diffraction pattern of LLTO/ZIF-8@IL/PEO clearly exhibits the corresponding signals from LLTO, ZIF-8, and PEO, providing strong evidence for its successful preparation. The magnified XRD patterns can be seen in Fig. S3 in the ESM, which show the typical diffraction peaks at 2θ = 7.4°, 12.8°, and 18.1°, further confirming the successful integration of ZIF-8 with LLTO. The TGA of various materials are exhibited in Fig. 3(b). Obviously, LLTO/ZIF-8@IL/PEO exhibits good thermal stability, with no mass loss occurring before 180 °C. Additionally, considering that PEO and IL-Li would completely decompose at 900 °C (Fig. S4 in the ESM), and based on the residual masses of different materials at this temperature, it can be calculated that LLTO/ZIF-8@IL/PEO consists of approximately 50.7 wt.% PEO matrix, 24.8 wt.% IL-Li, 22.6 wt.% LLTO, and 1.9 wt.% ZIF-8. For comparison, we also prepared the CSEs of LLTO/PEO, LLTO/ZIF-8/PEO, and LLTO/PEO-IL, formed by only incorporating LLTO with PEO, LLTO/ZIF-8 with PEO, and LLTO with PEO and IL-Li, respectively. The contents of LLTO, ZIF-8, and IL-Li in these samples are controlled to match those in LLTO/ZIF-8@IL/PEO. Figure 3(c) reveals the effect of incorporating different components on the melting point (T_m) of PEO through DSC. The incorporation of LLTO and ZIF-8 disrupts the ordering of PEO chains, resulting in the decrease in the melting point of PEO from 62.0 to 61.6 °C, and eventually to 60.5 °C. A sharp decrease to 46.3 °C is observed for LLTO/ZIF-8@IL/PEO, which can be attributed to the plasticizing effect of IL-Li. Besides, the differences in the mechanical properties of these electrolytes are reflected in the stress–strain

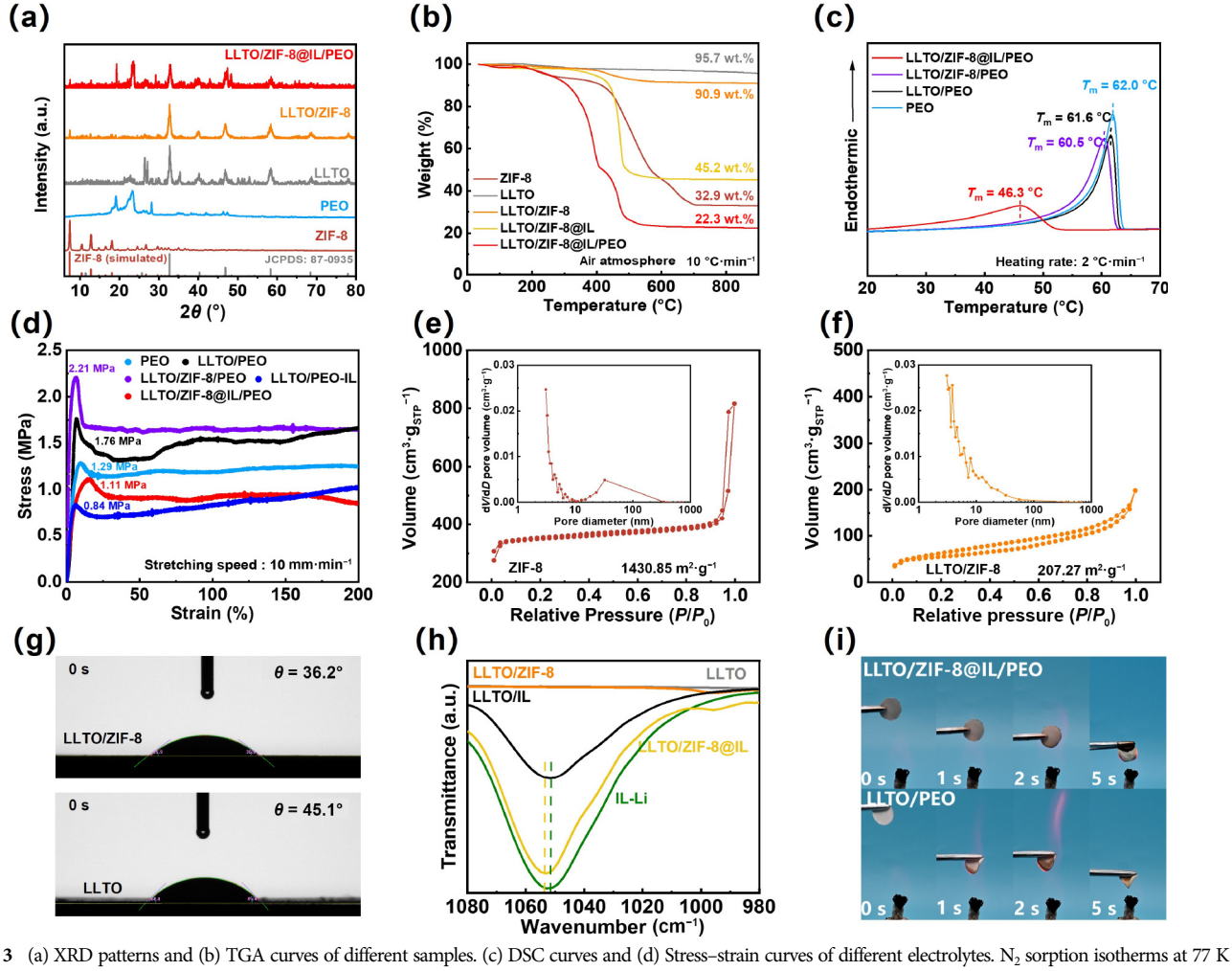

Figure 3 (a) XRD patterns and (b) TGA curves of different samples. (c) DSC curves and (d) Stress–strain curves of different electrolytes. N_2 sorption isotherms at 77 K for (e) ZIF-8 particles and (f) LLTO/ZIF-8 (inset: the corresponding pore size distributions). (g) Contact angle measurements with IL-Li for LLTO/ZIF-8 and LLTO at 0 s. (h) FTIR spectra of different samples ranging from 1080 to 980 cm^{-1} (dashed lines show absorption centers). (i) Digital photographs of LLTO/ZIF-8@IL/PEO and LLTO/PEO during the combustion test.

curves in Fig. 3(d). Obviously, the incorporation of inorganic components notably enhances the tensile strength of PEO, whereas IL-Li, acting as a plasticizer, reduces the tensile strength of LLTO/ZIF-8@IL/PEO. The specific surface areas of ZIF-8, LLTO, and LLTO/ZIF-8 are calculated to be 1430.85 $m^2 \cdot g^{-1}$ (Fig. 3(e)), 51.57 $m^2 \cdot g^{-1}$ (Fig. S5 in the ESM), and 207.27 $m^2 \cdot g^{-1}$ (Fig. 3(f)), respectively, further validating the successful integration of ZIF-8 particles onto the LLTO surface in LLTO/ZIF-8. Due to the strong affinity of ZIF-8 for IL-Li, LLTO/ZIF-8 exhibits a significantly lower initial contact angle with IL-Li compared to LLTO (Fig. 3(g)), and this trend remains consistent even after 5 s (Fig. S6 in the ESM). Furthermore, the FTIR spectra of LLTO, LLTO/ZIF-8, IL-Li, LLTO/IL (which represents the LLTO fiber absorbing IL-Li), and LLTO/ZIF-8@IL in the range of 1080 to 980 cm^{-1} are displayed in Fig. 3(h). A distinct blue shift from the peak at 1051 cm^{-1} in IL-Li and LLTO/IL to 1053 cm^{-1} in LLTO/ZIF-8@IL can be detected, which is induced by the mesoporous structure within ZIF-8 nanosizing the aggregated IL-Li clusters into ion pairs [33]. This phenomenon provides compelling evidence that IL-Li can be effectively infiltrated and trapped within the porous structure of ZIF-8. To further assess the practicality of the electrolytes under extreme conditions, combustion tests were conducted. The PEO electrolyte exhibits high flammability, with burning droplets dripping during combustion (Fig. S7 in the ESM). In contrast, LLTO/PEO maintains the structural integrity, while LLTO/ZIF-8@IL/PEO demonstrates the smallest flame and highest integrity (Fig. 3(i)), which can be attributed to the introduction of the IL with non-flammability feature.

Figure 4(a) shows the LSV curves of different electrolytes. Compared to PEO SE, LLTO/ZIF-8@IL/PEO exhibits an expanded electrochemical window of 4.7 V, owing to the inhibition of PEO end-group decomposition by LLTO and ZIF-8, along with the intrinsic high electrochemical stability of IL. The ionic conductivities of different CSEs at 60 °C can be calculated from the EIS results in Fig. 4(b). Compared to other CSEs, LLTO/ZIF-8@IL/PEO exhibits the highest ionic conductivity (1.07×10^{-3} $S \cdot cm^{-1}$), and its superior ion transport capability consistently outperforms other CSEs across the entire temperature range (Fig. 4(c) and Fig. S8 in the ESM). The activation energy (E_a) for ion transport of LLTO/ZIF-8@IL/PEO is calculated to be 0.45 eV, notably lower than those of LLTO/PEO (1.07 eV) and LLTO/ZIF-8/PEO (0.89 eV), indicating a reduced interfacial ion transport barrier across the organic–inorganic interface. The low E_a of LLTO/PEO-IL (0.38 eV) can be explained by the strong plasticizing effect of IL on the PEO electrolyte, which leads to the quasi-liquid-state ion transport within the PEO-IL matrix. In addition, the Li^+ transference number (t_{Li^+}) of LLTO/ZIF-8@IL/PEO is calculated to be 0.46 based on the chronoamperometry (CA) results (Fig. 4(d)), which is much higher than those of other CSEs (Fig. 4(e) and Fig. S9 in the ESM). This suggests that a greater proportion of Li^+ transport occurs through the LLTO phase, further confirming the reduction of the ion transport barrier across the PEO-LLTO interface. Compared to recent studies on enhancing interfacial ion transport in CSEs [34–38], LLTO/ZIF-8@IL/PEO achieves a relatively high ionic conductivity and t_{Li^+} (Fig. 4(f) and Table S1 in the ESM), underscoring the effectiveness of the confined solvation strategy. Notably, the performance comparison between LLTO/PEO-IL and LLTO/ZIF-8@IL/PEO reveals that the confinement effect of ZIF-8 can significantly reduce the adverse impact of IL-Li on the electrolyte. This effect ensures that IL-Li remains predominantly anchored on the LLTO surface rather than diffusing into the PEO matrix, thereby enhancing the mechanical properties and increasing the t_{Li^+} at the same time. To further evaluate the Li^+ exchange between LLTO and PEO, the ^7Li solid-state NMR and ^7Li-^7Li 2D EXSY NMR tests were performed on LLTO/PEO and LLTO/ZIF-8@IL/PEO. For LLTO/PEO, the PEO and LLTO electrolytes show two distinct peaks at −1.71 and 1.08 ppm (Fig. 4(g)), respectively. In contrast, the chemical shift of PEO remains unchanged in LLTO/ZIF-8@IL/PEO, while the peak of LLTO shifts to 0.92 ppm (Fig. 4(j)), which can be attributed to the increased electron cloud density induced by the introduction of the ZIF-8@IL layer. Further analysis of the ^7Li-^7Li 2D EXSY NMR spectra of the two electrolytes reveals that no off-diagonal cross-peaks are observed at the dashed box positions in LLTO/PEO (Fig. 4(h)), indicating that the ion exchange between LLTO and PEO is extremely slow, almost like being separated by a "canyon" (as illustrated in Fig. 4(i)). In contrast, the spectrum of LLTO/ZIF-8@IL/PEO shows clear cross-peaks at the dashed box positions (Fig. 4(k)), suggesting a significant enhancement in the Li^+ exchange rate between LLTO and PEO. A more vivid explanation is that Li^+ can "swim" through the "canyon" in a solvated form (Fig. 4(l)), facilitating their smooth transport from the PEO matrix to LLTO phase [39–45].

The stability of Li plating and stripping is a critical parameter for electrolytes. As shown in Fig. 5(a), the symmetric coin cells assembled with LLTO/PEO and LLTO/ZIF-8/PEO exhibit a gradually increasing overpotential during the Li plating/stripping cycles and eventually short-circuit. Thanks to the high ionic conductivity, the symmetric cell with LLTO/PEO-IL shows a stable cycling with low overpotential in the initial stage. However, it suddenly short-circuits after 362 h due to the degradation of mechanical properties caused by the plasticizing effect of IL (Fig. 3(d)). In sharp contrast, the symmetric cell with LLTO/ZIF-8@IL/PEO displays exceptional stability for over 1000 h. Besides, as shown in Fig. S10 in the ESM, compared to LLTO/PEO, the lithium foils disassembled from the symmetric cell with LLTO/ZIF-8@IL/PEO after 100 cycles exhibit a more uniform morphology. In addition, the symmetric cell with LLTO/ZIF-8@IL/PEO achieves a critical current density (CCD) of 0.5 $mA \cdot cm^{-2}$ (Fig. 5(b)), whereas the CCD values of LLTO/PEO-IL, LLTO/ZIF-8/PEO, and LLTO/PEO are only 0.4, 0.3, and 0.2 $mA \cdot cm^{-2}$, respectively (Fig. S11 in the ESM). To evaluate the practical application capability of different CSEs, they were assembled into Li||LFP coin cells for long-cycle and rate tests. As depicted in Figs. 5(c) and 5(e), the cell assembled with LLTO/ZIF-8@IL/PEO demonstrates outstanding long-cycle stability and rate performance compared to other CSEs. After 200 cycles at 1 C, the cell maintains a discharge capacity of 90.54 $mAh \cdot g^{-1}$ with a capacity retention of 69.35%. Notably, even at a high rate of 2 C, it still achieves a discharge capacity of 120 $mAh \cdot g^{-1}$. The corresponding charge–discharge curves are displayed in Figs. 5(d) and 5(f), exhibiting higher capacity and lower overpotential at the same cycle number and rate compared to LLTO/ZIF-8/PEO and LLTO/PEO (Figs. S12(b)–12(f) in the ESM). Notably, the charge–discharge curves of the Li||LFP coin cell assembled with LLTO/PEO-IL under 1 C (Fig. S12(a) in the ESM) show a slightly higher capacity and lower overpotential compared to LLTO/ZIF-8@IL/PEO at the initial cycle. Moreover, the charge–discharge curves of LLTO/PEO-IL at different C-rates (Fig. S12(b) in the ESM) exhibit similar capacity and overpotential to those of LLTO/ZIF-8@IL/PEO. This suggests that the plasticizing

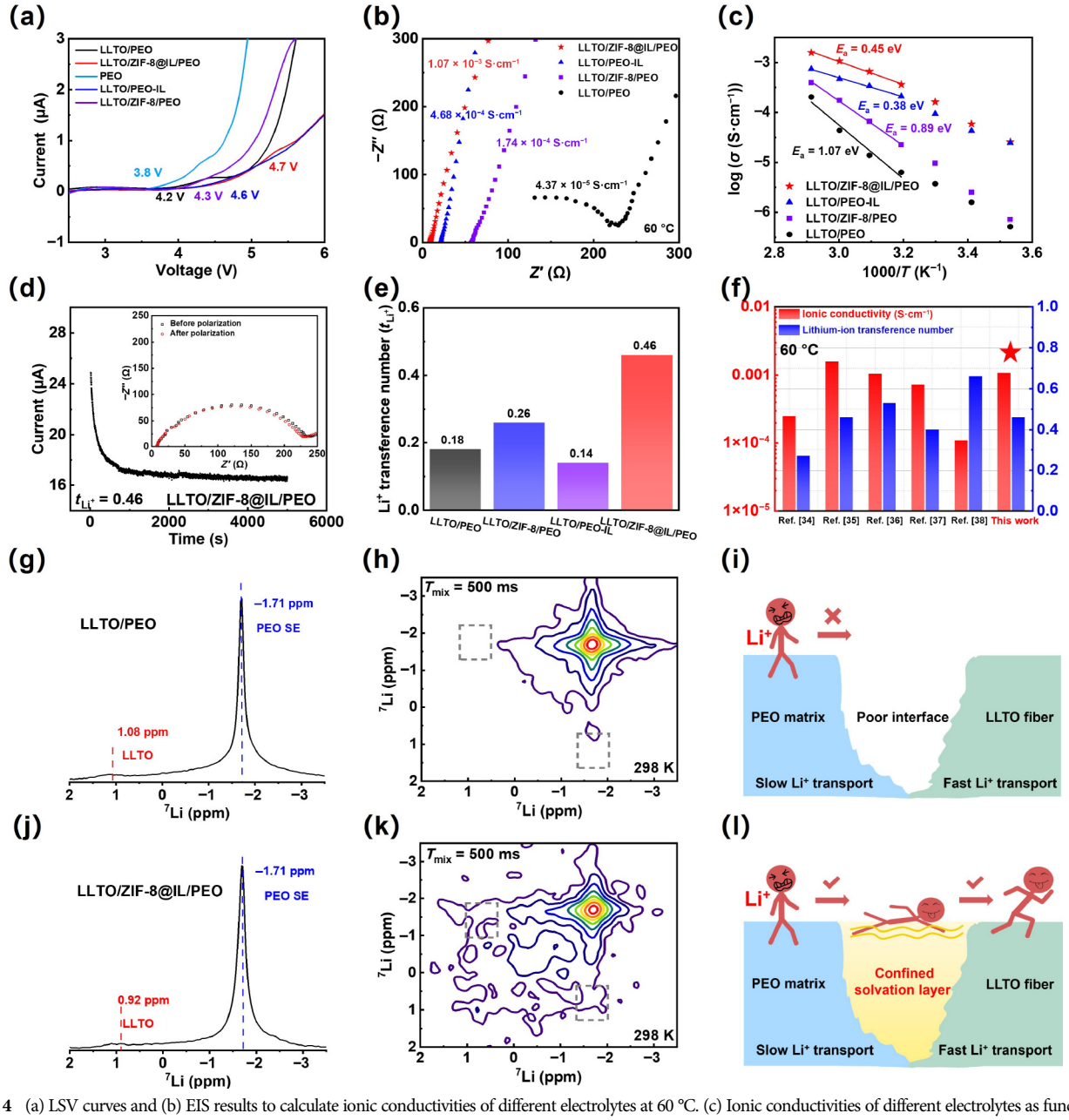

Figure 4 (a) LSV curves and (b) EIS results to calculate ionic conductivities of different electrolytes at 60 °C. (c) Ionic conductivities of different electrolytes as function of temperature ranging from 10 to 70 °C. (d) The CA curve for Li||LLTO/ZIF-8@IL/PEO||Li symmetrical cell (inset: EIS results of the cell before and after polarization). (e) Comparison of t_{Li^+} for different electrolytes. (f) Comparison of the ionic conductivity and t_{Li^+} of LLTO/ZIF-8@IL/PEO with values reported in recent literature. The ^{7}Li solid-state NMR spectra,^{7}Li-^{7}Li 2D EXSY NMR spectra, and the corresponding schematic of Li^+ transport across the interface of (g)–(i) LLTO/PEO and (j)–(l) LLTO/ZIF-8@IL/PEO.

effect of IL on PEO enhances the ionic conductivity and significantly improves the interfacial contact between the electrolyte and electrodes. However, this improvement comes at the expense of the reduced mechanical properties as evidenced in Fig. 3(d), which results in the inferior long-cycle performance in both Li||Li symmetric coin cells and Li||LFP coin cells. To further explore the potential applications of LLTO/ZIF-8@IL/PEO, the corresponding Li||LFP pouch cell with a LFP loading of 22 mg and Li||$LiCoO_2$ (LCO) coin cell with a higher charge–discharge plateau were assembled and evaluated. Encouragingly, the assembled Li||LFP pouch cell can deliver a discharge capacity of 135.02 mAh·g^{-1} over 100 cycles under 0.2 C (Fig. 5(g)) and successfully power the charging of a smartphone (Fig. 5(i)). Furthermore, as shown in Figs. 5(i) and 5(j), the Li||LCO coin cell assembled with LLTO/ZIF-8@IL/PEO exhibits stable cycling for 50 cycles at 0.2 C, retaining a capacity of 100 mAh·g^{-1}, highlighting the excellent compatibility of the electrolyte with high-voltage cathode materials. The relatively low Coulombic efficiency may be attributed to the inferior high-voltage tolerance of the PEO binder within the LCO cathode.

4 Conclusions

In summary, we successfully fabricated a novel CSE, denoted as LLTO/ZIF-8@IL/PEO, by introducing a confined solvation layer composed of ZIF-8 and IL-Li between the LLTO fibers and PEO electrolytes. This confined solvation layer can effectively convert the

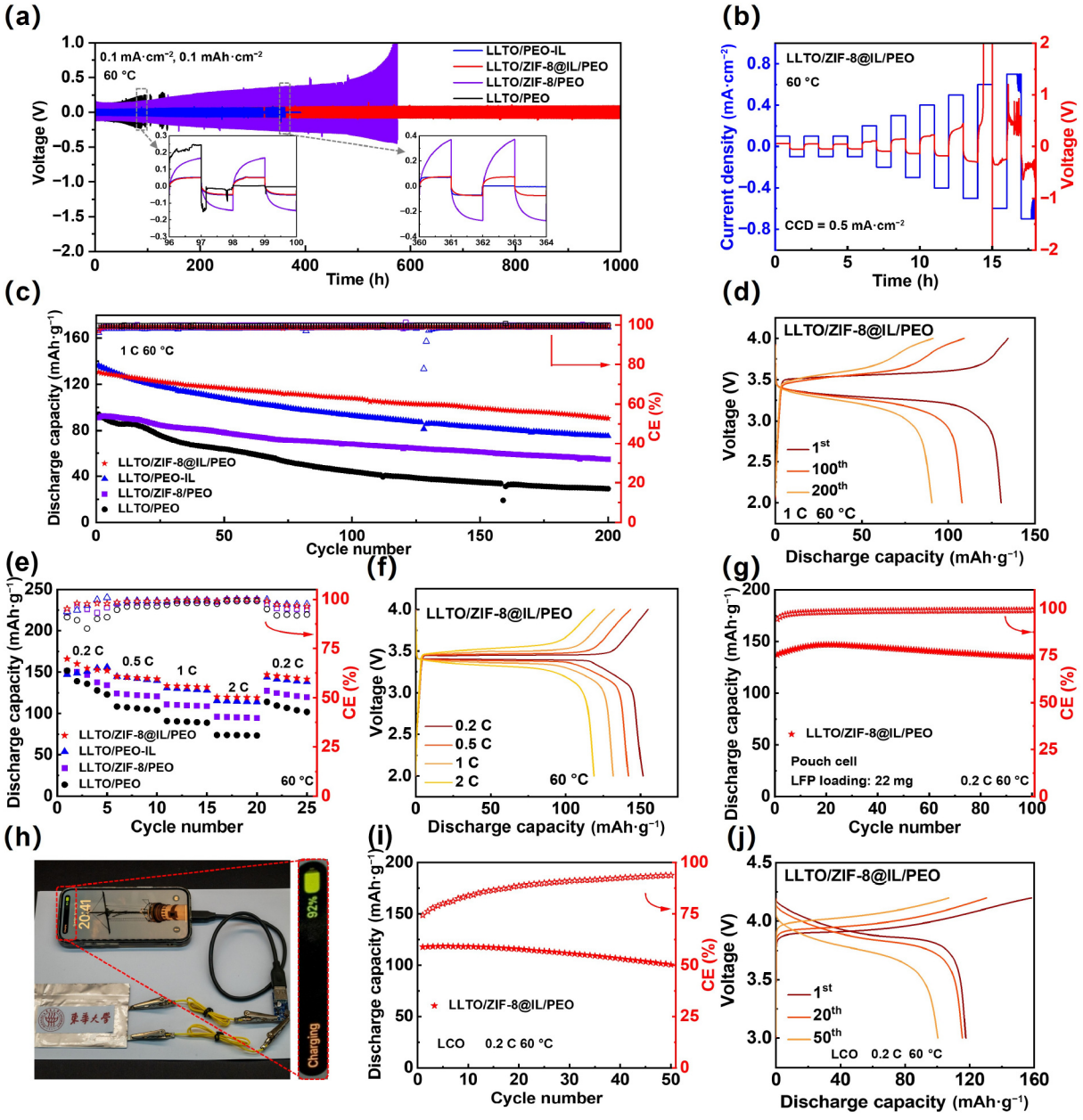

Figure 5 (a) Cycling performance of Li||Li symmetric coin cells assembled with different CSEs. (b) CCD tests of LLTO/ZIF-@IL/PEO. (c) Cycling and (e) rate performance of Li||LFP coin cells assembled with different CSEs. Charge–discharge curves for the Li||LFP coin cell assembled with LLTO/ZIF-@IL/PEO at (d) different cycle numbers and (f) C-rates. Cycling performance of (g) the Li||LFP pouch cell and (i) Li||LCO coin cell assembled with LLTO/ZIF-@IL/PEO. (h) The photograph showing the Li||LLTO/ZIF-@IL/PEO||LFP pouch cell charging a smartphone. (j) Charge–discharge curves for the Li||LCO coin cell assembled with LLTO/ZIF-@IL/PEO at different cycle numbers.

initially slow solid–solid interfacial Li^+ transport between LLTO and PEO into rapid solid–liquid interfacial Li^+ transport. Therefore, the advantage of LLTO has been fully exploited as fast Li^+ conducting fillers to significantly enhance the overall ionic conductivity of the LLTO/ZIF-8@IL/PEO electrolyte, which reaches 1.07×10^{-3} S·cm^{-1} 60 °C and exhibits a t_{Li^+} of 0.46. Encouragingly, the assembled Li||LFP pouch cell with a LFP loading of 22 mg can deliver a stable capacity of 135.02 mAh·g^{-1} under 0.2 C over 100 cycles at 60 °C and even power the charging of a smartphone. This confined solvation strategy provides a universal and convenient approach to improve the Li^+ transport across the organic–inorganic interface in CSEs, offering valuable insights for future research.

Electronic Supplementary Material: Supplementary material (EDS elemental mapping images, digital photographs, TGA curves, N_2 sorption isotherms, contact angle measurements, and EIS results of different samples, detailed charge–discharge curves of different cells) is available in the online version of this article at https://doi.org/10.26599/NR.2025.94907388.

Data availability

All data needed to support the conclusions in the paper are presented in the manuscript and the Electronic Supplementary Material. Additional data related to this paper may be requested from the corresponding author upon request.

Acknowledgements

This work acquired financial support from the National Natural Science Foundation of China (Nos. 52322302 and 22075042), the National Key Research and Development Program of China (No. 2023YFB3811902), the Fundamental Research Funds for the Central Universities (No. 2232024A-06), Shanghai Rising-Star Program (No. 22QA1400300), and Shanghai Scientific and Technological Innovation Project (No. 22520710100).

Declaration of competing interest

All the contributing authors report no conflict of interests in this work.

Author contribution statement

K. C.: Conceptualization, methodology, investigation, formal analysis, data curation, visualization, writing – original draft, writing – review & editing. M. J. L.: Investigation. X. X. L.: Investigation. F. L. L.: Writing – review & editing. C. Z.: Writing – review & editing. H. K. L.: Writing – review & editing. Y.-E. M.: Writing – review & editing, supervision, funding acquisition. T. X. L.: Writing – review & editing, supervision, funding acquisition. All the authors have approved the final manuscript.

Use of AI statement

None.

References

[1] Zheng, Y.; Yao, Y. Z.; Ou, J. H.; Li, M.; Luo, D.; Dou, H. Z.; Li, Z. Q.; Amine, K.; Yu, A. P.; Chen, Z. W. A review of composite solid-state electrolytes for lithium batteries: Fundamentals, key materials and advanced structures. *Chem. Soc. Rev.* **2020**, *49*, 8790–8839.

[2] Utomo, N. W.; Hong, S. F.; Sinha, R.; Kim, K. I.; Deng, Y.; Ochonma, P.; Kitahata, M. G.; Garcia-Mendez, R.; Joo, Y. L.; Archer, L. A. Solid-state polymer-particle hybrid electrolytes: Structure and electrochemical properties. *Sci. Adv.* **2024**, *10*, eado4719.

[3] Zhao, W. J.; Yi, J.; He, P.; Zhou, H. S. Solid-state electrolytes for lithium-ion batteries: Fundamentals, challenges and perspectives. *Electrochem. Energy Rev.* **2019**, *2*, 574–605.

[4] Ngai, K. S.; Ramesh, S.; Ramesh, K.; Juan, J. C. A review of polymer electrolytes: Fundamental, approaches and applications. *Ionics* **2016**, *22*, 1259–1279.

[5] Wang, Z. X.; Liu, R.; Ba, Z. H.; Xu, K.; Li, X. T.; Dong, J.; Zhang, Q. H.; Zhao, X. Built-in garnet-rich composite solid electrolyte towards fast ion transport and dendrite-free for high-energy lithium batteries. *Compos. Commun.* **2024**, *47*, 101871.

[6] Guo, Y.; Wu, S. C.; He, Y. B.; Kang, F. Y.; Chen, L. Q.; Li, H.; Yang, Q. H. Solid-state lithium batteries: Safety and prospects. *eScience* **2022**, *2*, 138–163.

[7] Wang, J. H.; Han, X. J.; Feng, Y. F.; Chen, S.; Yuan, H.; Yang, R. X.; Du, W.; Hou, C. X.; Liu, X.; Tong, T. et al. *In-situ* construction of a composite interlayer for dendrite-free $Li_{6.75}La_3Zr_{1.75}Ta_{0.25}O_{12}$ solid-state batteries. *Compos. Commun.* **2024**, *46*, 101851.

[8] Song, X.; Ma, K.; Wang, H.; Wang, J.; Chen, J. W.; Zheng, Z. M.; Zhang, J. M. Enhancing Li^+ transfer efficiency and strength of PEO-based composite solid electrolyte for long stable cycling of all-solid-state lithium metal batteries. *Compos. Commun.* **2024**, *50*, 102013.

[9] Wang, M. X.; Lv, S. W.; Li, M. X.; Li, X.; Li, C. P.; Li, Z. L.; Chen, X. C.; Wu, J. X.; Li, X. Y.; Chen, Y. M. et al. A heterogeneous quasi-solid-state hybrid electrolyte constructed from electrospun nanofibers enables robust electrode/electrolyte interfaces for stable lithium metal batteries. *Adv. Fiber Mater.* **2024**, *6*, 727–738.

[10] Li, Z.; Huang, H. M.; Zhu, J. K.; Wu, J. F.; Yang, H.; Wei, L.; Guo, X. Ionic conduction in composite polymer electrolytes: Case of PEO: Ga-LLZO composites. *ACS Appl. Mater. Interfaces* **2019**, *11*, 784–791.

[11] Zhu, L.; Zhu, P. H.; Fang, Q. X.; Jing, M. X.; Shen, X. Q.; Yang, L. Z. A novel solid PEO/LLTO-nanowires polymer composite electrolyte for solid-state lithium-ion battery. *Electrochim. Acta* **2018**, *292*, 718–726.

[12] Cao, X. W.; Ma, C.; Luo, L.; Chen, L.; Cheng, H.; Orenstein, R. S.; Zhang, X. W. Nanofiber materials for lithium-ion batteries. *Adv. Fiber Mater.* **2023**, *5*, 1141–1197.

[13] Yu, Y.; Liu, M.; Chen, Z. Y.; Zhang, Z. H.; Qiu, T.; Hu, Z. X.; Xiang, H. X.; Zhu, L. P.; Xu, G. Y.; Zhu, M. F. Advances in nonwoven-based separators for lithium-ion batteries. *Adv. Fiber Mater.* **2023**, *5*, 1827–1851.

[14] Lin, D. C.; Liu, W.; Liu, Y. Y.; Lee, H. R.; Hsu, P. C.; Liu, K.; Cui, Y. High ionic conductivity of composite solid polymer electrolyte via *in situ* synthesis of monodispersed SiO_2 nanospheres in poly(ethylene oxide). *Nano Lett.* **2016**, *16*, 459–465.

[15] Zhang, X. K.; Xie, J.; Shi, F. F.; Lin, D. C.; Liu, Y. Y.; Liu, W.; Pei, A.; Gong, Y. J.; Wang, H. X.; Liu, K. et al. Vertically aligned and continuous nanoscale ceramic-polymer interfaces in composite solid polymer electrolytes for enhanced ionic conductivity. *Nano Lett.* **2018**, *18*, 3829–3838.

[16] Shi, P. R.; Ma, J. B.; Liu, M.; Guo, S. K.; Huang, Y. F.; Wang, S. W.; Zhang, L. H.; Chen, L. K.; Yang, K.; Liu, X. T. et al. A dielectric electrolyte composite with high lithium-ion conductivity for high-voltage solid-state lithium metal batteries. *Nat. Nanotechnol.* **2023**, *18*, 602–610.

[17] Huo, H. Y.; Zhao, N.; Sun, J. Y.; Du, F. M.; Li, Y. Q.; Guo, X. X. Composite electrolytes of polyethylene oxides/garnets interfacially wetted by ionic liquid for room-temperature solid-state lithium battery. *J. Power Sources* **2017**, *372*, 1–7.

[18] Xu, Y. N.; Wang, K.; Zhang, X. D.; Ma, Y. B.; Peng, Q. F.; Gong, Y.; Yi, S.; Guo, H.; Zhang, X.; Sun, X. Z. et al. Improved li-ion conduction and (electro)chemical stability at garnet-polymer interface through metal-nitrogen bonding. *Adv. Energy Mater.* **2023**, *13*, 2204377.

[19] Chen, L. K.; Shi, P. R.; Gu, T.; Mi, J. S.; Yang, K.; Zhao, L.; Lv, J. S.; Liu, M.; He, Y. B.; Kang, F. Y. Strategies of constructing highly stable interfaces with low resistance in inorganic oxide-based solid-state lithium batteries. *eScience* **2025**, *5*, 100277.

[20] Huo, H. Y.; Li, X. N.; Sun, Y. P.; Lin, X. T.; Doyle-Davis, K.; Liang, J. W.; Gao, X. J.; Li, R. Y.; Huang, H.; Guo, X. X. et al. Li_2CO_3 effects: New insights into polymer/garnet electrolytes for dendrite-free solid lithium batteries. *Nano Energy* **2020**, *73*, 104836.

[21] Simon, F. J.; Hanauer, M.; Richter, F. H.; Janek, J. Interphase formation of PEO_{20}: LiTFSI-Li_6PS_5Cl composite electrolytes with lithium metal. *ACS Appl. Mater. Interfaces* **2020**, *12*, 11713–11723.

[22] Liu, M.; Zhang, S. N.; van Eck, E. R. H.; Wang, C.; Ganapathy, S.; Wagemaker, M. Improving Li-ion interfacial transport in hybrid solid electrolytes. *Nat. Nanotechnol.* **2022**, *17*, 959–967.

[23] Jia, M. Y.; Bi, Z. J.; Shi, C.; Zhao, N.; Guo, X. X. Air-stable dopamine-treated garnet ceramic particles for high-performance composite electrolytes. *J. Power Sources* **2021**, *486*, 229363.

[24] Zhan, X.; Pang, X. K.; Mao, F. Q.; Lin, J. D.; Li, M.; Zhao, Y. H.; Xu, P.; Xu, Z. M.; Liao, K. M.; Zhang, Q. B. et al. Interfacial reconstruction unlocks inherent ionic conductivity of Li-La-Zr-Ta-O garnet in organic polymer electrolyte for durable room - temperature all - solid - state batteries. *Adv. Energy Mater.* **2024**, *14*, 2402509.

[25] Yılmazoğlu, M.; Okkay, H.; Abaci, U.; Coban, O. High-performance PVdF-HFP/PEG-IL composites: The combined effects of PEG and ionic liquid on proton conductivity and dielectric characteristics. *Compos. Commun.* **2025**, *53*, 102175.

[26] Forsyth, M.; Porcarelli, L.; Wang, X. E.; Goujon, N.; Mecerreyes, D.

Innovative electrolytes based on ionic liquids and polymers for next-generation solid-state batteries. *Acc. Chem. Res.* **2019**, *52*, 686–694.
[27] Wang, Y. Y.; Pan, T.; Yuan, G. Q.; Li, Q.; Pang, H. MOF and MOF-derived composites for flexible energy storage devices. *Compos. Commun.* **2024**, *52*, 102144.
[28] Wang, Z. T.; Zhou, H.; Meng, C. F.; Xiong, W. W.; Cai, Y. J.; Hu, P. F.; Pang, H.; Yuan, A. H. Enhancing ion transport: Function of ionic liquid decorated MOFs in polymer electrolytes for all-solid-state lithium batteries. *ACS Appl. Energy Mater.* **2020**, *3*, 4265–4274.
[29] Yu, X. W.; Grundish, N. S.; Goodenough, J. B.; Manthiram, A. Ionic liquid (IL) laden metal-organic framework (IL-MOF) electrolyte for quasi-solid-state sodium batteries. *ACS Appl. Mater. Interfaces* **2021**, *13*, 24662–24669.
[30] Wang, Z. Q.; Tan, R.; Wang, H. B.; Yang, L. Y.; Hu, J. T.; Chen, H. B.; Pan, F. A Metal-organic-framework-based electrolyte with nanowetted interfaces for high-energy-density solid-state lithium battery. *Adv. Mater.* **2018**, *30*, 1704436.
[31] Wang, Z. Y.; Du, Z. J.; Liu, Y. Y.; Knapp, C. E.; Dai, Y. H.; Li, J. W.; Zhang, W.; Chen, R. W.; Guo, F.; Zong, W. et al. Metal-organic frameworks and their derivatives for optimizing lithium metal anodes. *eScience* **2024**, *4*, 100189.
[32] Yang, Y.; Wu, Q.; Wang, D.; Ma, C. C.; Chen, Z.; Su, Q. T.; Zhu, C. Z.; Li, C. H. Ionic liquid enhanced composite solid electrolyte for high-temperature/long-life/dendrite-free lithium metal batteries. *J. Membr. Sci.* **2020**, *612*, 118424.
[33] Fujie, K.; Yamada, T.; Ikeda, R.; Kitagawa, H. Introduction of an ionic liquid into the micropores of a metal-organic framework and its anomalous phase behavior. *Angew. Chem., Int. Ed.* **2014**, *53*, 11302–11305.
[34] Zhang, Y. X.; Yu, X. H.; Li, X. X.; Ren, J. G.; He, P.; Zhang, C.; Teng, C. Q.; Miao, Y. E.; Liu, T. X. LLZTO crosslinks form a highly stretchable self-healing network for fast healable all-solid lithium metal batteries. *Chem. Eng. J.* **2024**, *497*, 154397.
[35] Zhang, X. R.; Liu, S. Y.; Sun, Y. X.; Gao, L. J.; Chen, K.; Dong, F. L.; Sun, H.; Xie, H. M.; Liu, J. Surface coordination of garnet fillers improves the organic-inorganic interfacial compatibility of composite solid electrolyte. *Small* **2024**, *20*, 2405909.
[36] Wei, L. Y.; Feng, Y.; Ge, S. H.; Liu, S. J.; Ma, Y. Y.; Yan, J. H. Three-dimensionally printed ionogel-coated ceramic electrolytes for solid-state lithium batteries. *ACS Nano* **2025**, *19*, 5789–5800.
[37] Jiang, Y.; Chen, K.; He, J. P.; Sun, Y. X.; Zhang, X. R.; Yang, X. X.; Xie, H. M.; Liu, J. A self-healing composite solid electrolyte with dynamic three-dimensional inorganic/organic hybrid network for flexible all-solid-state lithium metal batteries. *J. Colloid Interface Sci.* **2025**, *678*, 200–209.
[38] Chen, W. P.; Duan, H.; Shi, J. L.; Qian, Y. M.; Wan, J.; Zhang, X. D.; Sheng, H.; Guan, B.; Wen, R.; Yin, Y. X. et al. Bridging interparticle Li^+ conduction in a soft ceramic oxide electrolyte. *J. Am. Chem. Soc.* **2021**, *143*, 5717–5726.
[39] Lang, Z. Q.; Wang, X. X.; Jabeen, S.; Cheng, Y. Y.; Liu, N. Y.; Liu, Z. H.; Gan, T.; Zhuang, Z. C.; Li, H. T.; Wang, D. S. Destabilization of single-atom catalysts: Characterization, mechanisms, and regeneration strategies. *Adv. Mater.* **2025**, *37*, 2418942.
[40] Hao, J. C.; Wang, T. D.; Cai, J.; Gao, G. H.; Zhuang, Z. C.; Yu, R. H.; Wu, J. S.; Wu, G. M.; Lu, S. L.; Wang, X. F. et al. Suppression of structural heterogeneity in high-entropy intermetallics for electrocatalytic upgrading of waste plastics. *Angew. Chem., Int. Ed.* **2025**, *64*, e202419369.
[41] Meng, G.; Huang, Z. M.; Tao, L.; Zhuang, Z. C.; Zhang, Q. C.; Chen, Q. L.; Yang, H.; Zhao, H. P.; Ye, C. L.; Wang, Y. et al. Atomic symbiotic-catalyst for low-temperature zinc-air battery. *Angew. Chem., Int. Ed.*, in press, https://doi.org/10.1002/anie.202501649.
[42] Kang, Q.; Zhuang, Z. C.; Li, Y.; Zuo, Y. Z.; Wang, J.; Liu, Y. J.; Shi, C. Q.; Chen, J.; Li, H. F.; Jiang, P. K. et al. Manipulating dielectric property of polymer coatings toward high-retention-rate lithium metal full batteries under harsh critical conditions. *Nano Res.* **2023**, *16*, 9240–9249.
[43] Xiao, X. F.; Zhuang, Z. C.; Yin, S. H.; Zhu, J. X.; Gan, T.; Yu, R. H.; Wu, J. S.; Tian, X. C.; Jiang, Y. X.; Wang, D. S. et al. Topological transformation of microbial proteins into iron single-atom sites for selective hydrogen peroxide electrosynthesis. *Nat. Commun.* **2024**, *15*, 10758.
[44] Sun, Q.; Zeng, G. F.; Xu, X.; Li, J.; Biendicho, J. J.; Wang, S.; Tian, Y. H.; Ci, L. J.; Cabot, A. Are sulfide-based solid-state electrolytes the best pair for Si anodes in Li-ion batteries. *Adv. Energy Mater.* **2024**, *14*, 2402048.
[45] Zhang, S. N.; Sun, Q.; Martínez-Alanis, P. R.; Chen, G. W.; Li, J. W.; Zeng, G. F.; Biendicho, J. J.; Ci, L. J.; Cabot, A. Towards flame retardant high-performance solid-state lithium metal batteries: Poly(ionic liquid)-based lithiophilic ion-conductive interfaces and humidity tolerant binders. *Nano Energy* **2025**, *133*, 110424.